Chinese Chemical Letters 34 (2023) 108152

Contents lists available at ScienceDirect

Chinese Chemical Letters

journal homepage: www.elsevier.com/locate/cclet

Prussian blue analogue derived $NiCoSe_4$ coupling with nitrogen-doped carbon nanofibers for pseudocapacitive electrodes

Guohao Yang[a,b,1], Chengang Pei[c,1], Fang Xu[a,*], Ho–Seok Park[c], Xu Yu[d,*], Huan Pang[d,*]

[a] School of Material Science and Engineering, Guizhou Minzu University, Guiyang 550025, China
[b] School of Chemical Engineering, Guizhou Minzu University, Guiyang 550025, China
[c] Department of Chemical Engineering, College of Engineering, Sungkyunkwan University, Suwon-si, Gyeonggi-do 440-746, Republic of Korea
[d] School of Chemistry and Chemical Engineering, Yangzhou University, Yangzhou 225002, China

ARTICLE INFO

Article history:
Received 5 December 2022
Revised 23 December 2022
Accepted 12 January 2023
Available online 13 January 2023

Keywords:
Electrospinning
Carbon nanofibers
Supercapacitors
Heteroatom doping
Metal selenides

ABSTRACT

The design of pseudocapacitive materials by coupling transition metal compounds with a conductive carbon matrix is important for the high performance of supercapacitors. Herein, we construct the Prussian blue analogue derived nickel-cobalt selenides coupling with nitrogen-doped carbon nanofibers ($NiCoSe_4$-NCNFs) by carbonization and selenization of polyacrylonitrile nanofibers. The effect of selenization and element N doping on the morphological structure and surface chemistry of $NiCoSe_4$-NCNFs are evaluated. Due to the accelerated electrolyte ion diffusion, enlarged active surface area and the modified surface chemistry by the strong interaction at $NiCoSe_4$/NCNFs interfaces, $NiCoSe_4$-NCNFs show excellent capacitive behaviors in 1 mol/L KOH, and the specific capacitance is 1257 F/g at 1 A/g with a rate capability of 78% and cyclic stability of 82.9%. The Gibbs free energy of adsorption OH^- is calculated by density functional theory to investigate the charge storage mechanism. This work offers a new strategy to construct the transition metal selenides/carbon nanofibers hybrids for high-performance supercapacitor devices.

The combustion of fossil fuels results in serious environmental problems and the aim to get rid of the energy crisis is a global concern [1,2]. Supercapacitors (SCs) own the merits of high-power density, long-term stability, and less susceptibility to overheating at high charge/discharge rates, which are one promising energy storage system to satisfy the energy demand [3–5]. Pseudocapacitors (PCs) arise from the reversible redox reactions by the accommodation of charges at or near the electrode surface [6–9]. However, the low energy density is still the dominant limitation of PCs in practical applications. The effort on developing conspicuous electrode materials is an effective strategy to enhance the energy density.

Prussian blue analogue (PBA) as one member of metal-organic frameworks owns the merits of abundant porosity and uniform element distribution [10,11], and PBA-derived transition metal oxides (TMO) as pseudocapacitive electrode materials have attracted attention due to their rich faradic reaction and large specific surface area [12–14]. To overcome their low electrical conductivity, the electronic structure modification of TMO by heteroatoms doping has been reported, such as sulfidation and phosphidation [15–17]. Cubic NiS nanoframes and hollow nickel cobalt phosphate with nitrogen-doped carbon show improved capacitive behaviors [16,17]. Recently, transition metal selenides (TMS) with excellent capacitive behaviors attract attention. Selenium has similar physical and chemical properties with sulfur and oxygen [18,19] and a larger atomic size than sulfur [20], which result in a smaller band gap and larger polarizability of TMS than TMO [21]. The replacement of oxygen sites by selenide species is the primary motivation to explore pseudocapacitive materials. Furthermore, the introduction of a conductive matrix as the second functional component can increase the cyclic stability of electrode materials.

Carbon-based nanomaterials (carbon nanotubes, graphene) have received extensive attention as conductive materials attributing to their high electrical conductivity [22–25]. The hybrids by incorporating TMO with graphene, carbon nanotubes have been constructed to show the enhanced electrochemical performance, such as MnO_2/graphene [5] and $Co(OH)_2$/carbon nanotube [26]. One-dimensional (1D) carbon nanofibers (CNFs) obtained from the electrospinning technique own large surface-volume ratios and efficient ion/electron transport [27–29]. After stabilization and carbonization, CNFs with high porosity and the rough surface can expose more specific surfaces and accelerate the electrolyte ion diffusion. It was well known that the performance of electrode materi-

* Corresponding authors.
E-mail addresses: vivi_fang1211@126.com (F. Xu), yxypz15@yzu.edu.cn (X. Yu), panghuan@yzu.edu.cn (H. Pang).
[1] These authors contributed equally to this work.

https://doi.org/10.1016/j.cclet.2023.108152
1001-8417/

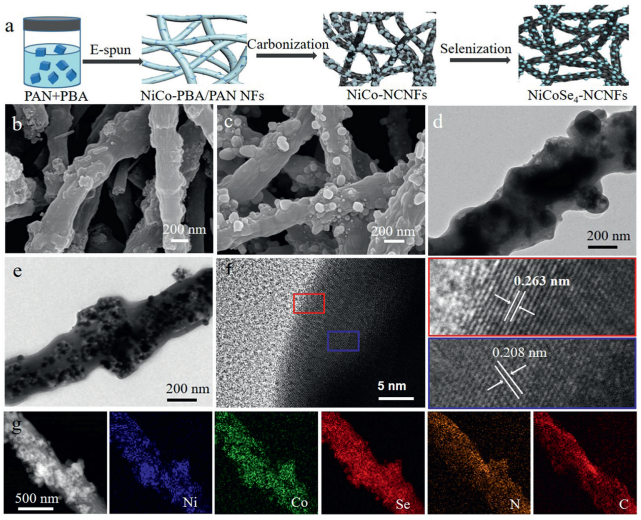

Fig. 1. (a) Schematic illustration of the preparation process of $NiCoSe_4$-NCNFs. SEM images of (b) NiCo-NCNFs and (c) $NiCoSe_4$-NCNFs. TEM images of (d) NiCo-NCNFs and (e) $NiCoSe_4$-NCNFs. (f) HR-TEM image and (g) elemental mapping of $NiCoSe_4$-NCNFs.

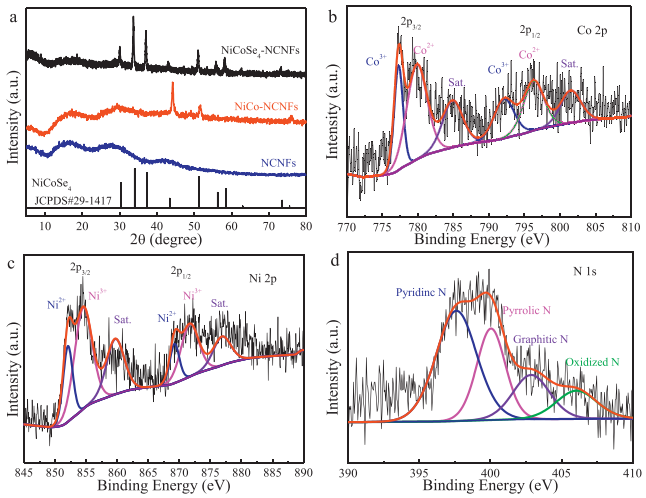

Fig. 2. (a) XRD patterns of NCNFs, NiCo-NCNFs, $NiCoSe_4$-NCNFs. High-resolution XPS spectra of $NiCoSe_4$-NCNFs, (b) Co 2p, (c) Ni 2p and (d) N 1s.

als is strong relative to their morphological structure and chemical composition. Heteroatom-doped CNFs with excellent capacitive performance have been reported. The incorporation of heteroatoms into carbon materials can adjust the electronic structure to improve the electrochemical performance of SCs, such as N-doped CNFs [30] and P-doped CNFs [31]. The hybridization of CNFs with TMS or TMO is an attractive strategy to construct the highly active materials to achieve excellent capacitive performance, such as NiO nanoparticles with N doped CNFs [32]; CNFs wrapped NiS nanoparticles [33] and hollow Co_3O_4 embedded CNFs [34]. Therefore, the design of one-dimensional hybrid by coupling PBA-derived bimetallic selenides with heteroatom N doping carbon is necessary to be explored as highly pseudocapacitive materials for SCs.

Herein, we prepared the nickel-cobalt selenides coupled with nitrogen-doped carbon nanofibers ($NiCoSe_4$-NCNFs) *via* the selenization and carbonization of the electrospun NiCo PBA/polyacrylonitrile (PAN) nanofibers. The $NiCoSe_4$ nanoparticles and N-doped CNFs are the dominant pseudocapacitive materials. Due to the synergistic effect of porous 1D structure and the hybridization of bimetallic selenides with NCNFs, $NiCoSe_4$-NCNFs exhibit excellent capacitive behaviors for SCs in 1 mol/L KOH, such as the high specific capacitance (1257 F/g), good rate capability (78%) and cyclic stability (82.9%). This work presents an effective design concept for constructing 1D bimetallic selenides with heteroatom-doped CNFs as promising pseudocapacitive materials for SCs.

Fig. 1a shows the schematic illustration of $NiCoSe_4$-NCNFs by electrospinning, thermal activation and selenization approaches. The homogeneity of the polymer dispersion is an important factor to electrospun the uniformly distributed 1D nanofibers. The average size of NiCo-PBA is about 200 nm (Fig. S1 in Supporting information). The homogeneous dispersion of NiCo-PBA/PAN is obtained due to their good dispersibility in dimethylformamide (DMF). The well-aligned 1D nanofibers are obtained without forming the beads. The polymer is decomposed to ammonia gas at 800 °C, which acts as the nitrogen source to construct the NCNFs. Finally, the $NiCoSe_4$-NCNFs are obtained after the carbonization and selenization of NiCo-PBA/PAN nanofibers.

The morphological structure of $NiCoSe_4$-NCNFs is characterized by scanning electron microscopy (SEM). NiCo-PBA/PAN nanofibers exhibit raised surface, which is different from pristine PAN nanofibers (Fig. S2 in Supporting information). After the carbonization at 800 °C, the polymer nanofibers are decomposed into NCNFs (Fig. S2c) and NiCo-NCNFs (Fig. 1b). NiCo-NCNFs show the cracked and collapsed structure of PBA nanocubes by the reduction of metal ions. Especially, the formation of metal selenides for $NiCoSe_4$-NCNFs results in the rough surface morphology and the stable decoration of nanoparticles on or beneath the NCNFs surfaces (Fig. 1c).

As confirmed by transmission electron microscopy (TEM), NiCo-PBA nanocubes are evenly wrapped in PAN nanofibers for NiCo-PBA/PAN, which is different from the smooth surface of PAN nanofibers (Fig. S3 in Supporting information). The raised bump and rough surface are caused by embedding the PBA nanocubes beneath the surface of PAN nanofibers. After carbonization at 800 °C, the transparent phenomena for NiCo-NCNFs disappears attributing to the formation of small-sized NiCo species and nitrogen-doped carbon nanofibers (Fig. 1d). The increased diameter of $NiCoSe_4$-NCNFs is attributed to the formation of metal selenides on or beneath the surface of nanofibers (Fig. 1e). The increased surface roughness and porosity of nanofibers are conductive to provide abundant pathways for fast ion diffusion. Furthermore, the high-resolution TEM image of $NiCoSe_4$-NCNFs shows the interplanar spacing of 0.263 and 0.208 nm, corresponding to the (210) and (220) planes of $NiCoSe_4$ (Fig. 1f), respectively. The energy-dispersive X-ray spectra (EDX) confirms the existence of Ni, Co, Se, N and C elements in Fig. S4 (Supporting information). The distribution of Ni, Co, Se, N and C elements is well-matched with the outline of $NiCoSe_4$-NCNFs (Fig. 1g), implying the successful construction of heteroatom N doping and the formation of metal selenides.

The structure and crystallinity of $NiCoSe_4$-NCNFs were confirmed by X-ray diffraction (XRD) in Fig. 2a. The peak at 27° for NCNFs corresponds to the (002) plane of graphitic carbon [35], and the intensity is decreased for $NiCoSe_4$-NCNFs due to the formation metal compounds. Meanwhile, the diffraction peaks of NiCo-NCNFs correspond to the typical planes of NiCo alloys [36]. The peaks at 33.7°, 37.1° and 43.4° for $NiCoSe_4$-NCNFs are related to the (210), (211), and (220) planes of $NiCoSe_4$ (JCPDS No. 29–1417). This result proves the successful construction of metal selenides during the activation treatment. The formation of defective sites after N doping and selenization was confirmed by Raman spectra in Fig. S5 (Supporting information), and a larger ID/IG ratio of $NiCoSe_4$-NCNFs than that of NiCo-NCNFs and NCNFs implying more exposed surface area and active site for fast faradic reaction.

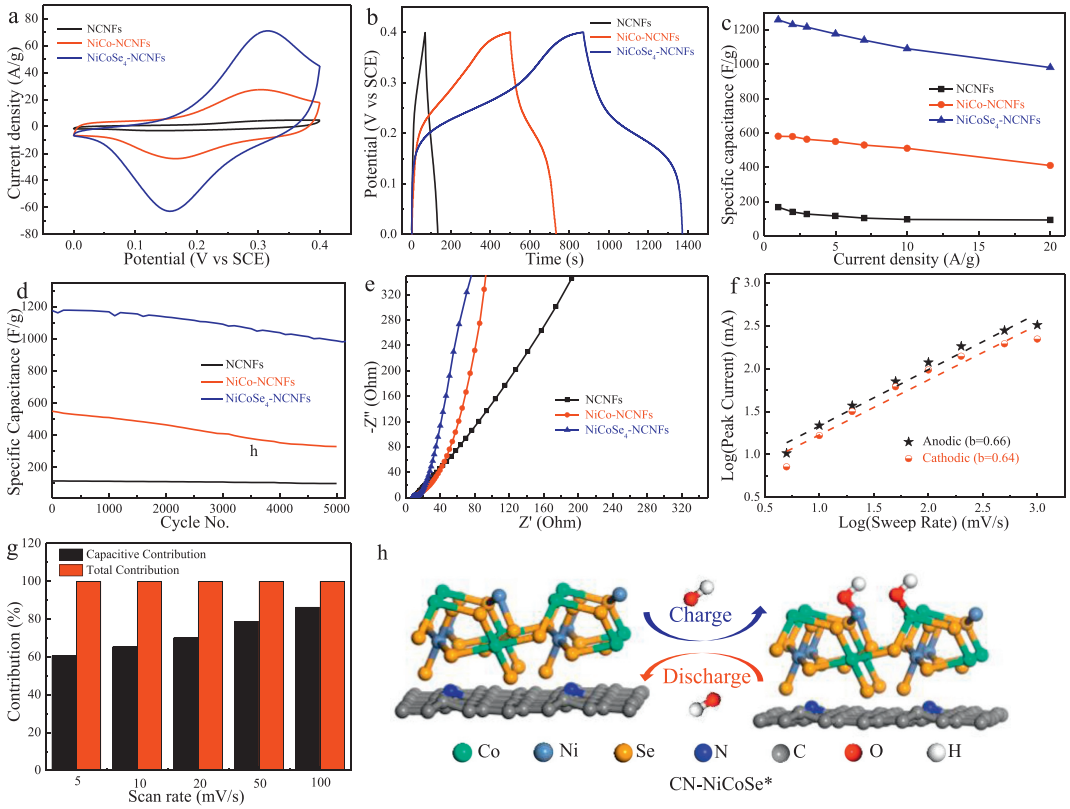

Fig. 3. (a) CV curves at 50 mV/s, (b) GCD curves at 1 A/g, (c) rate capability, (d) cyclic stability and (e) Nyquist plots of NCNFs, NiCo-NCNFs and $NiCoSe_4$-NCNFs. (f) The calculated *b* values by plotting log(sweep rate) *vs.* log(peak current). (g) The capacitive and diffusive contribution of $NiCoSe_4$-NCNFs at different scan rates. (h) The geometry-optimized structure of CN-NiCoSe* before and after OH adsorbed at the active sites.

The chemical composition of $NiCoSe_4$-NCNFs was probed by X-ray photoelectron spectroscopy (XPS). $NiCoSe_4$-NCNFs are composed of Ni, Co, Se, N and C elements (Fig. S6 and Table S1 in Supporting information). The deconvoluted peaks of Co 2p at 777.3 and 779.9 eV correspond to Co^{3+} and Co^{2+} of Co $2p_{3/2}$, and the peaks at 792.2 and 796.4 eV ascribe to the Co^{3+} and Co^{2+} of Co $2p_{1/2}$, accompanying the related satellite peaks (Fig. 2b), respectively [37]. The deconvoluted Ni 2p spectra show two peaks at 852.1 and 869.2 eV for Ni^{2+} and two peaks at 854.7 and 871.8 eV for Ni^{3+} in Fig. 2c, respectively [38]. For Se 3d spectra in Fig. S7 (Supporting information), the peaks at 54.1, 54.8 and 57.9 eV correspond to Se $3d_{5/2}$, Se $3d_{3/2}$ and the oxidation state of selenides. The existent oxygen groups for $NiCoSe_4$-NCNFs can be attributed to the surface oxidation by exposing sample under air conditions [39,40]. In comparsion, the oxygen content for $NiCoSe_4$-NCNFs is much lower than that of NiCo-NCNFs implying a high electrical conductivity for $NiCoSe_4$-NCNFs, which is favorable for improving the capacitive performance. During the thermal activation process, the diffusion of electrons is from the metallic Ni/Co center to the non-metallic Se center to improve the synergistic effect in $NiCoSe_4$ composites [41]. The formation of pyridinic-N and pyrrolic-N bond in implyies the successful incorporation of N into carbon (Fig. 2d), which is further confirmed by C 1s spectra in Fig. S8 (Supporting information). The pyridinic and pyrrolic N have been proven as effective active sites for fast faradic reactions [42]. The formation of NiCo selenides and N-doped carbon are favorable for improving the capacitive performance of $NiCoSe_4$-NCNFs [43].

The electrochemical behaviors of $NiCoSe_4$-NCNFs were measured by cyclic voltammetry (CV) in 1 mol/L KOH by a three-electrode configuration in Fig. 3a. $NiCoSe_4$-NCNFs own apparent redox peaks and large current density at 50 mV/s, indicating a highly reversible pseudocapacitive performance. As the scan rate increased from 5 mV/s to 100 mV/s, the symmetrical CV curves for $NiCoSe_4$-NCNFs indicate the reversible redox reaction during the charge/discharge process (Fig. S9 in Supporting information). Meanwhile, $NiCoSe_4$-NCNFs show higher redox peaks than that of NiCo-NCNFs, resulting from the formation of metal selenides as the dominant active sites for fast faradic reactions. The corresponding redox reaction during the charge-discharge process for $NiCoSe_4$ is typically presented as follows [44]:

$$NiCoSe_4 + 2OH^- \rightleftharpoons NiSe_2OH + CoSe_2OH + 2e^- \quad (1)$$

$$CoSe_2OH + OH^- \rightleftharpoons CoSe_2O + H_2O + e^- \quad (2)$$

$$NiSe_2OH + OH^- \rightleftharpoons NISe_2O + H_2O + e^- \quad (3)$$

Galvanostatic charge/discharge (GCD) curves were further carried out at various current densities, and the distorted symmetric GCD curves for $NiCoSe_4$-NCNFs at 1 A/g imply their pseudocapacitive behavior in Fig. 3b. The calculated specific capacitance of $NiCoSe_4$-NCNFs (1257 F/g) is 2.1 and 7.9 times higher than that of NiCo-NCNFs (585 F/g) and NCNFs (168 F/g), respectively. The specific capacitance of $NiCoSe_4$-NCNFs maintains a value of 980 F/g with a rate capability of 78% from 1 A/g to 20 A/g (Fig. S10 in Supporting information), which is larger than that of NiCo-NCNFs (70.8%) and NCNFs (55.6%) in Fig. 3c. The stability of pseudocapacitive $NiCoSe_4$-NCNFs is confirmed by GCD curves at 5 A/g for 5000 cycles in Fig. 3d. The capacitance retention is 82.9% for $NiCoSe_4$-NCNFs, which is much larger than that of NiCo-NCNFs (60.2%). The slow decay in specific capacitance for $NiCoSe_4$-NCNFs can be ascribed to the effective accommodation of electrons on the active surface where the fast reversible redox reaction occurs. The excellent long-term stability of $NiCoSe_4$-NCNFs is further confirmed

by CV test for 5000 cycles at 100 mV/s (Fig. S11 in Supporting information). The kinetic behavior of $NiCoSe_4$-NCNFs is evaluated by electrochemical impedance spectroscopy (EIS) in Fig. 3e. And the equivalent series resistance (ESR) is obtained by the intercept of Nyquist plot in the high frequency, arising from the electrolyte resistance. The charge transfer resistance (R_{ct}) for $NiCoSe_4$-NCNFs (1.36 Ω) is smaller than NiCo-NCNFs (3.2 Ω) and NCNFs (2.14 Ω). This result demonstrates that $NiCoSe_4$-NCNFs have fast kinetic behaviors at the electrode/electrolyte interface due to the strong interfacial connection between $NiCoSe_4$ and NCNFs.

The electrochemical reaction kinetics of $NiCoSe_4$-NCNFs are studied by Dunn's methods [45], and the charge storage mechanism can be divided into the capacitive and diffusive dominant process. Especially, the occurrence of faradic reaction at the electrode surface means that the capacitive contribution is dominant, and the diffusive contribution is dominant whereas the faradic reaction occurs inside the bulk electrode [46,47]. The *b* values of 0.5 and 1.0 imply the diffusion-controlled and capacitive-controlled processes as the related dominant charge storage mechanism. The capacitive contribution of $NiCoSe_4$-NCNFs is studied by the redox peak current (i) with the related scan rate (v) [48]. The *b* value is 0.66 and 0.64 for the anodic and cathodic peaks of $NiCoSe_4$-NCNFs in Fig. 3f, indicating the dominant capacitive-controlled process. At 5 mV/s, the percentage of capacitive contribution for $NiCoSe_4$-NCNFs is about 60.5%, which is dramatically increased to 86.2% at 100 mV/s (Fig. 3g and Fig. S12 in Supporting information). As further confirmed by Trasatti's method, the capacitive contribution is calculated to 62.3% for $NiCoSe_4$-NCNFs by maximum surface capacitance divided by maximum total capacitance in Fig. S13 (Supporting information). These evidences confirm that the diffusive restriction can be hindered by coupling pseudocapacitive metal selenides with NCNFs. The capacitive-controlled mechanism for $NiCoSe_4$-NCNFs with fast reversible faradic reactions is suitable for application in the high-power energy system. The charge storage mechanism of $NiCoSe_4$-NCNFs was further elucidated by density function theory (DFT) calculation. The more negative energy of OH adsorption (E_{ads}) predicts stronger binding at the active sites. The E_{ads} value of the simulated CN-NiCoSe* (−1.89 eV) is more negative than that of CN-NiCo* (−1.78 eV) and CN* (−0.75 eV) in Fig. 3h and Fig. S14 (Supporting information), respectively. The simulated CN-NiCoSe* model would be the most dominant active site for reversible and fast charge transfer.

The electrochemical performance of the assembled $NiCoSe_4$-NCNFs||$NiCoSe_4$-NCNFs supercapacitors was tested in 1 mol/L Na_2SO_4 with the enlarged potential window of 1.5 V. Fig. 4a shows the CV curves of the symmetric supercapacitor at 50 mV/s under different potentials, and the potential window of 1.5 V is finally chosen because of the appearance of electrolyte decomposition at 1.6 V. Fig. 4b shows the CV curves of $NiCoSe_4$-NCNFs||$NiCoSe_4$-NCNFs supercapacitors at scan rates from 5 mV/s to 100 mV/s. The distorted rectangular shape of CV curves implies the good reversibility of $NiCoSe_4$-NCNFs. The specific capacitance is 81 F/g at 0.5 A/g and the capacitance retention is about 58% from 0.5 A/g to 5 A/g in Fig. 4c, which are both higher than those of NiCo-NCNFs (Fig. S15 in Supporting information). The ESR for $NiCoSe_4$-NCNFs||$NiCoSe_4$-NCNFs arises from the contact interface between electrode and electrolyte (Fig. S16 in Supporting information), and the calculated R_{ct} value is 23.5 Ω. The Ragone diagram of $NiCoSe_4$-NCNFs||$NiCoSe_4$-NCNFs is calculated from the GCD curves in Fig. 4d and the maximum energy density can be delivered to 58.6 Wh/kg with the power density of 864 W/kg.

Herein, $NiCoSe_4$-NCNFs were prepared by electrospinning, carbonization and selenization. The rough surface and crosslinked structure are helpful for electrolyte ion diffusion and increase the active surface area. Meanwhile, the surface chemistry is modified by forming metal selenides and heteroatoms N doping into CNFs.

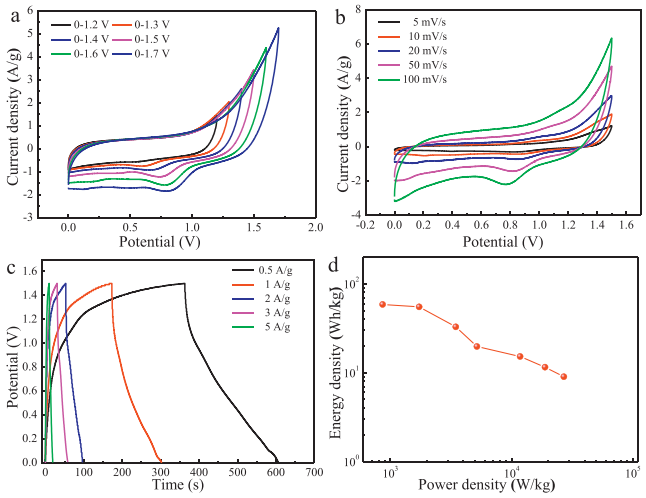

Fig. 4. (a) CV curves of $NiCoSe_4$-NCNFs||$NiCoSe_4$-NCNFs supercapacitors at 50 mV/s under different potentials. (b) CV, (c) GCD curves at 1.5 V and (d) Ragone plot of $NiCoSe_4$-NCNFs||$NiCoSe_4$-NCNFs.

Due to the synergistic effect of morphological structure and chemical composition, $NiCoSe_4$-NCNFs show excellent capacitive behavior of SCs. The charge storage mechanism of $NiCoSe_4$-NCNFs is demonstrated by Dunn's method and DFT calculation. This work provides a guideline for constructing the coupling of the PBA-derived material with carbon nanofibers for high performance of SCs.

Declaration of competing interest

The authors declare that they have no known competing financial interests or personal relationships that could have appeared to influence the work reported in this paper.

Acknowledgments

The work is supported by the Science and Technology Foundation of Guizhou Provincial Department of Education, China (No. KY[2018]147). X. Yu also thanks the Six Talent Peaks Project of Jiangsu Province (No. XCL-103) and "High-End Talent Project" of Yangzhou University. We also acknowledge the technical support at the Testing Center of Yangzhou University.

Supplementary materials

Supplementary material associated with this article can be found, in the online version, at doi:10.1016/j.cclet.2023.108152.

References

[1] T. Chen, L. Dai, Mater. Today 16 (2013) 272–280.
[2] Z. Wu, L. Li, J.M. Yan, X.B. Zhang, Adv. Sci. 4 (2017) 1600382.
[3] A.G. Pandolfo, A.F. Hollenkamp, J. Power Sources 157 (2006) 11–27.
[4] Z. Xiong, P. Hu, Y. Zhang, et al., J. Electron. Mater. 47 (2018) 5987–5992.
[5] X. Meng, L. Lu, C. Sun, ACS Appl. Mater. Interfaces 10 (2018) 16474–16481.
[6] J. Zhou, S. Zhang, Y.N. Zhou, et al., Electrochem. Energy Rev. 4 (2021) 219–248.
[7] Z. Xu, W. Deng, X. Wang, Electrochem. Energy Rev. 4 (2021) 269–335.
[8] C. Costentin, T.R. Porter, J.M. Savéant, ACS Appl. Mater. Interfaces 9 (2017) 8649–8658.
[9] J. Xiao, L. Wan, S. Yang, F. Xiao, S. Wang, Nano Lett. 14 (2014) 831–838.
[10] W.J. Li, C. Han, G. Cheng, et al., Small 15 (2019) 1900470.
[11] B. Singh, A. Indra, Mater. Today Energy 16 (2020) 100404.
[12] H. Ju, X.D. Liu, C.Y. Tao, et al., J. Alloy. Compd. 856 (2021) 157134.
[13] G. Yan, X. Zhang, L. Xiao, J. Mater. Sci. 54 (2019) 7087–7095.
[14] J.S. Gao, Z. Liu, Y. Lin, et al., Chem. Eng. J. 388 (2020) 124368.
[15] H. Ju, X.D. Liu, C.Y. Tao, et al., Electrochim. Acta 366 (2021) 137410.
[16] X.Y. Yu, L. Yu, H.B. Wu, X.W. Lou, Angew. Chem. Int. Ed. 127 (2015) 5421–5425.
[17] L. Xu, Y. Xi, W. Li, et al., Nano Energy 91 (2022) 106630.

[18] T.W. Lin, C.S. Dai, K.C. Hung, Sci. Rep. 4 (2014) 7274.
[19] Y.N. Ko, S.H. Choi, Y.C. Kang, ACS Appl. Mater. Interfaces 8 (2016) 6449–6456.
[20] Z. Jin, H. Nie, Z. Yang, et al., Nanoscale 4 (2012) 6455–6460.
[21] X.F. Wang, C.C. Pei, Q. Wang, et al., Inorg. Chem. Front. 9 (2022) 547–558.
[22] A.M. Zardkhoshoui, S.S.H. Davarani, Chem. Eng. J. 402 (2020) 126421.
[23] J.W. Wang, M.Z. Li, Y. Zhai, et al., Appl. Surf. Sci. 556 (2021) 149789.
[24] S. Ghosh, P. Samanta, N.C. Murmu, T. Kuila, J. Alloy. Compd. 835 (2020) 155432.
[25] J.W. Miao, Q.Z. Zhu, K.L. Li, et al., J. Energy Chem. 52 (2021) 243–250.
[26] C. Wang, H. Qu, T. Peng, et al., Electrochim. Acta 191 (2016) 133–141.
[27] Z.Y. Tang, X.H. Shang, B. Hu, et al., Carbon 187 (2022) 47–55.
[28] B.H. Kim, C.H. Kim, K.S. Yang, A. Rahy, D.J. Yang, Electrochim. Acta 83 (2012) 335–340.
[29] D.X. Cheng, Y.H. Li, J.L. Zhang, et al., Carbon 170 (2020) 527–542.
[30] X. Tian, N. Zhao, Y. Song, et al., Electrochim. Acta 185 (2015) 40–51.
[31] Y. Li, Y. Liu, M. Wang, et al., Carbon 130 (2018) 377–383.
[32] Q. Li, J. Guo, D. Xu, et al., Small 14 (2018) 1704203.
[33] J. Xu, L. Zhang, G. Xu, et al., Appl. Surf. Sci. 434 (2018) 112–119.
[34] F. Zhang, C. Yuan, J. Zhu, et al., Adv. Funct. Mater. 23 (2013) 3909–3915.
[35] W. Wang, W. Zhang, G. Wang, C. Li, J. Mater. Chem. A 9 (2021) 15766–15775.
[36] Y. Fu, H.Y. Yu, C. Jiang, et al., Adv. Funct. Mater. 28 (2018) 1705094.
[37] Y. Zhao, J.H. Zheng, M. Yuan, et al., J. Alloy. Compd. 885 (2021) 160866.
[38] A.M. Zardkhoshoui, S.S.H. Davarani, Nanoscale 12 (2020) 12476–12489.
[39] J. Balamurugan, T.T. Nguyen, V. Aravindan, et al., Nano Energy 65 (2019) 103999.
[40] G. Nagaraju, S.M. Cha, S.C. Sekhar, J.S. Yu, Adv. Energy Mater. 7 (2017) 1601362.
[41] Y.Q. Sun, K. Xu, Z.X. Wei, et al., Adv. Mater. 30 (2018) 1802121.
[42] M Xu, Y. Liu, Q. Yu, et al., Chin. Chem. Lett. 32 (2021) 184–199.
[43] S. Li, Y.J. Ruan, Q. Xie, Electrochim. Acta 356 (2020) 136837.
[44] J. Zhao, H. Cheng, Z.H. Zhang, et al., Adv. Funct. Mater. 32 (2022) 2202063.
[45] J. Wang, J. Polleux, J. Lim, B. Dunn, J. Phys. Chem. C 111 (2007) 14925–14931.
[46] W.S. Chen, X. Yu, Z.X. Zhao, S.C. Ji, L.G. Feng, Electrochim. Acta 298 (2019) 313–320.
[47] K. Brezesinski, J. Wang, J. Haetge, et al., J. Am. Chem. Soc. 132 (2010) 6982–6990.
[48] M. Jia, Y.H. Jin, P.Z. Zhao, et al., Electrochim. Acta 310 (2019) 230–239.